Chemical Engineering Journal 496 (2024) 154040

Contents lists available at ScienceDirect

Chemical Engineering Journal

journal homepage: www.elsevier.com/locate/cej

Stacked dual-interface bi-hydrophilic structuration boosting solar vapor-to-water conversion

Shuai Peng [a,1], Shi-Hai Deng [b,1], Longqian Xu [a,c], Huu Hao Ngo [d,*], Pengkang Jin [b], Wenshan Guo [d], Zuofeng Chen [e], Deli Wu [a,f,*]

[a] State Key Laboratory of Pollution Control and Resources Reuse, College of Environmental Science & Engineering, Tongji University, Shanghai 200092, China
[b] School of Human Settlements and Civil Engineering, Xi'an Jiaotong University, Xi'an 710049, China
[c] Department of Civil and Environmental Engineering, Vanderbilt University, Nashville, TN, USA
[d] Centre for Technology in Water and Wastewater, School of Civil and Environmental Engineering, University of Technology Sydney, Sydney, NSW 2007, Australia
[e] Shanghai Key Lab of Chemical Assessment and Sustainability, Department of Chemistry, Tongji University, Shanghai 200092, China
[f] Shanghai Institute of Pollution Control and Ecological Security, Shanghai 200092, China

ARTICLE INFO

Keywords:
Enthalpy recovery
Front-end evaporation architecture
Efficient water collection
Anti-fogging
Specific water productivity

ABSTRACT

Generating solar vapor through thermal localization is a promising solution to address the global water shortage. However, incident light attenuation and latent heat accumulation of front-end condensing interface have led to a negative cascade effect between low condensing efficiency and heat loss, constraining the water evaporation rates (WER) and specific water productivity (SWP). This study presents an innovative approach of stacked front-end heat recovery architecture (SFE-HRA) developed based on a bi-hydrophilic transparent micro-nano-film (biH-TMNF). The biH-TMNF is designed and functionalized as a circulatable front-end vapor condensation cooling component that integrates a liquid film condensation module with two-phase functionalization and a porous hydrogel module. The biH-TMNF allows solar vapors from the bottom to adhere to the anti-fogging hydrophilic surface as a micro-liquid film while maintaining as high a light incidence as possible ($>$ 90 %). At the same time, the latent heat of vapor is released to the second stage of the transparent hydrogel evaporator to drive the next stage of the latent heat of the vapor cycle. A 3-stage stacked SFE-HRA was constructed and demonstrated with the conventional solar evaporator [(SFE-HRA)-CSE]. The (SFE-HRA)-CSE system obtained a considerable increase in water evaporation rates (WER) by 150 % and a substantial improvement in condensate recovery by 200–300 %. A critical role of the dual bi-hydrophilic interface has been emphasized in promoting the efficiencies of latent heat cycle and water harvesting. The proof-of-concept testing confirmed an unprecedented SWP efficiency of 130 % from (SFE-HRA)-CSE, surpassing all SWPs from the high-performance front-end evaporators that have been reported.

1. Introduction

With over half of the global population experiencing water scarcity, utilizing natural sunlight for seawater desalination offers a sustainable solution [1,2]. However, existing solar desalination systems either demand complex infrastructure or need more energy efficiency, hindering their widespread implementation [3,4]. Even when operating at thermodynamic limits, large-scale installations would be necessary to meet the average daily drinking water demand of 2.5 L per person [5,6].

Researchers pioneered the concept of solar vapor generation through heat localization, and subsequent efforts have focused on improving water evaporation rates (WER) by enhancing optical absorption [7–10], minimizing heat loss [11,12], optimizing water supply [13], reducing evaporation enthalpy, and constructing cold evaporation surfaces [14–17]. Despite these advancements, a significant gap remains between the increased solar evaporation rate and the persistently low specific water productivity (SWP) [18–22]. SWP per unit of area and time is a crucial metric in solar-driven desalination and is predominantly

---

* Corresponding authors at: Centre for Technology in Water and Wastewater, School of Civil and Environmental Engineering, University of Sydney, Sydney NSW 2007, Australia (H.H. Ngo); State Key Laboratory of Pollution Control and Resources Reuse, College of Environmental Science & Engineering, Tongji University, Shanghai 200092, China (D. Wu).

E-mail addresses: huuhao.ngo@uts.edu.au (H.H. Ngo), wudeli@tongji.edu.cn (D. Wu).

[1] Both authors contributed equally.

https://doi.org/10.1016/j.cej.2024.154040
Received 2 May 2024; Received in revised form 5 July 2024; Accepted 14 July 2024

affected by vapor condensation rather than vapor generation [6]. Therefore, there is a pressing need for innovative approaches or technologies to improve SWP and bridge the research gap in solar-driven desalination.

The front-end evaporator's inherent structural features, which integrate evaporation and light absorption on the same side, present challenges in optimizing heat and mass transfer [23]. The challenges are particularly evident in vapor collection and condensation processes, resulting in approximately 26 % of incident solar energy dissipated into the environment [24–26] and exhibiting low SWP rates of 0.75–1 kg $m^{-2}h^{-1}$ and only 30–50 % solar-to-water conversion efficiency [18]. Furthermore, single-stage distillation cycles face inherent thermodynamic limits, with a theoretical upper limit of water production rate at 1.47 [l $m^{-2}h^{-1}$] for a 1 kW m^{-2} energy flux [6,27,28]. To increase the water production rate per unit of light concentration, efficiently reusing latent heat and incorporating multiple condensation processes hold significant potential [29–35]. However, existing research on front-end solar evaporators has mainly worked on the optimisation of vapor generation performance, an overall system design and corresponding material strategy that can balance the conflict between solar vapor generation and efficient condensation water production has not been explored [36–41]. Overcoming this limitation is crucial for achieving commercially competitive decentralized water production [30].

Given the challenges above, this work develops an innovative active solar vapor-water recovery system utilizing bi-hydrophilic transparent micro-nano films (biH-TMNF) with dual interfaces. This device enables front-end multi-stage solar evaporation and water recovery by capitalizing on the anti-light attenuation properties of liquid film condensation at the lower interface of the stacked front-end heat recovery architecture (SFE-HRA), as well as the accelerated interface evaporation facilitated by the porous hydrogel skeleton at the upper interface. Through comprehensive mechanistic modelling and experimental characterization, we demonstrate the versatility of integrating a three-stage stacked SFE-HRA (100 cm^2) with a conventional solar evaporator. This integration yields a significant enhancement in solar vapor production and achieves an impressive SWP and SWP efficiency. This research presents new solutions for efficient front-end solar vapor-to-water recovery through the design and optimization of the materials, optics, heat dissipation, and structure of the SFE-HRA device. It holds promising potential for addressing the challenges associated with sustainable water production through solar energy.

2. Materials and methods

2.1. Experimental materials

Poly (vinyl alcohol) (PVA, Mw = 195,000 g mol^{-1}), hydrochloric acid (37 % HCl, 1.2 mol/L) and glutaraldehyde (50 wt% aqueous solutions) were provided by Aladdin Chemistry Co. Ltd., China. Commercial polymer resin anti-fog film (thickness of 0.0504 mm, haze of 0.5 %, 180° peel strength of 500 g $inch^{-1}$, visible light transmission rate of 90 %) was supplied by Run Xia Co. Ltd. (China). A transparent polymethyl methacrylate frame (inner diameter of 10 cm, outer diameter of 12 cm, thickness of 1 mm) was purchased from INTE Trading Co. Ltd. (China). Heat-resistant silicone mats (temperature resistance range –60 °C – +220 °C, specific gravity 1.3, shore hardness 50) were supplied by Chasing Wind Metal Products Co. Ltd. (China). A pneumatic airbrush (TG180, nozzle diameter of 0.2 mm, working pressure of 15–50 psi) was purchased from TAGORE Machinery Co. Ltd. (China). Black polyvinyl chloride membrane (elongation at break 200 %, temperature resistance range: 90 °C–130 °C) was purchased from Hao Tie Electronic Technology Co. Ltd. (China). Cotton fibre nonwoven (~0.2 mm thick, with a superficial density of ~0.08 kg m^{-2}) was purchased from Ou Sheng Hong Trading Co. Ltd. (China). All chemicals in this study were of analytical reagent grade, and all the materials were used without further purification. The physical and chemical properties of all materials are from official product descriptions.

2.2. Characterization of WPH and AFM

The morphology of the WPHs was analyzed by SEM (Hitachi Regulus 8100). A contact angle goniometer (Dataphysics DCAT21) was used to characterize the hydrophobic and hydrophilic properties of the WPHs and AFM. A UV–vis-NIR spectrophotometer equipped with an integrating sphere was used to detect the reflectance (R) and transmission (T) spectra of the solar absorber layer of the black absorber (Shimadzu UV-3600), and the absorption was then calculated (A=1 – R – T). Thermography images were obtained using an infrared camera ((FLIR TG-267). ATR-FTIR spectra were collected by Thermo Scientific Nicolet iS20 instrument assisted by ATR attachments. The Horiba Lab RAM HR Evolution instrument compiled Raman spectra. Simultaneous thermal analyzer TG-DSC tested the enthalpy of evaporation of WPH samples and pure water. 3D morphology and roughness of WPH films were analyzed by laser microscopy (KEYENCE VK-X150). Surface roughness and thickness of anti-fog film were characterized by atomic force microscopy (Bruker Dimension Icon).

2.3. Preparation of SFE-HRA frame

Each SFE-HRA framework is assembled from biH-TMNF and adjustable-thickness acrylic hollow fixation components (INTE Trading Co. Ltd). Different SFE-HRA sizes are obtained by adjusting the dimensions of the biH-TMNF pre-coated framework and the thickness of the flexible silicone pad. The construction method of biH-TMNF with desired size and structure is described in Supplementary Note 2.2. AFM acts as an intermediate layer, with the non-fogging layer facing the silicone pad, creating a fixed AFM framework. The pre-synthesized PVA solution is crosslinked onto the non-fogging side of the AFM through combing scrape coating and in-situ fogging polymerization using an electrostatic spray gun. After gelation for 12 h, the initial biH-TMNF framework is transferred to a pre-cooled freeze dryer (SCIENTZ-18ND) and frozen for 8 h at minus 58 °C, allowing vertical growth of ice crystals within the gel. The biH-TMNF is dried for 24 h at room temperature in an airtight environment to prepare a tight-fitting biH-TMNF. In the assembly process, the edges of the partially dried biH-TMNF membranes are wrapped in transparent waterproof tape to prevent substrate deformation by overheating.

2.4. COMSOL simulation

The model is applied to describe a laminar drying gas stream through a WPH sample with different morphological characteristics, simulating a porous medium containing wet air and liquid water. Fluid flow, phase change heat transfer and transport physical fields of the involved liquid and gas are added, and all these effects are strongly coupled. Based on the amounts of water vapor and dry air, the mixing law is used to describe the transport and thermodynamic properties of air containing water vapor, and the compressible Navier-Stokes equations are solved to calculate the velocity and pressure fields for the free flow of heat and moisture convection transport. The basic principles of simulating two-phase flow in porous media are similar. Inside the WPH samples, the relative humidity decreases from 100 % everywhere to 10 % under ambient air conditions. The main parameters set in the simulation processes are shown in Supplementary Note 2.4. The simulation conditions were consistent for the above morphologies when not otherwise stated.

2.5. Solar-thermal evaporation measurements

Evaporation experiments were conducted using a 300 W xenon lamp with an AM 1.5 G filter to simulate solar flux output (HF-GHX-XE-300). The solar flux (200–11,000 nm) was measured using a solar power meter

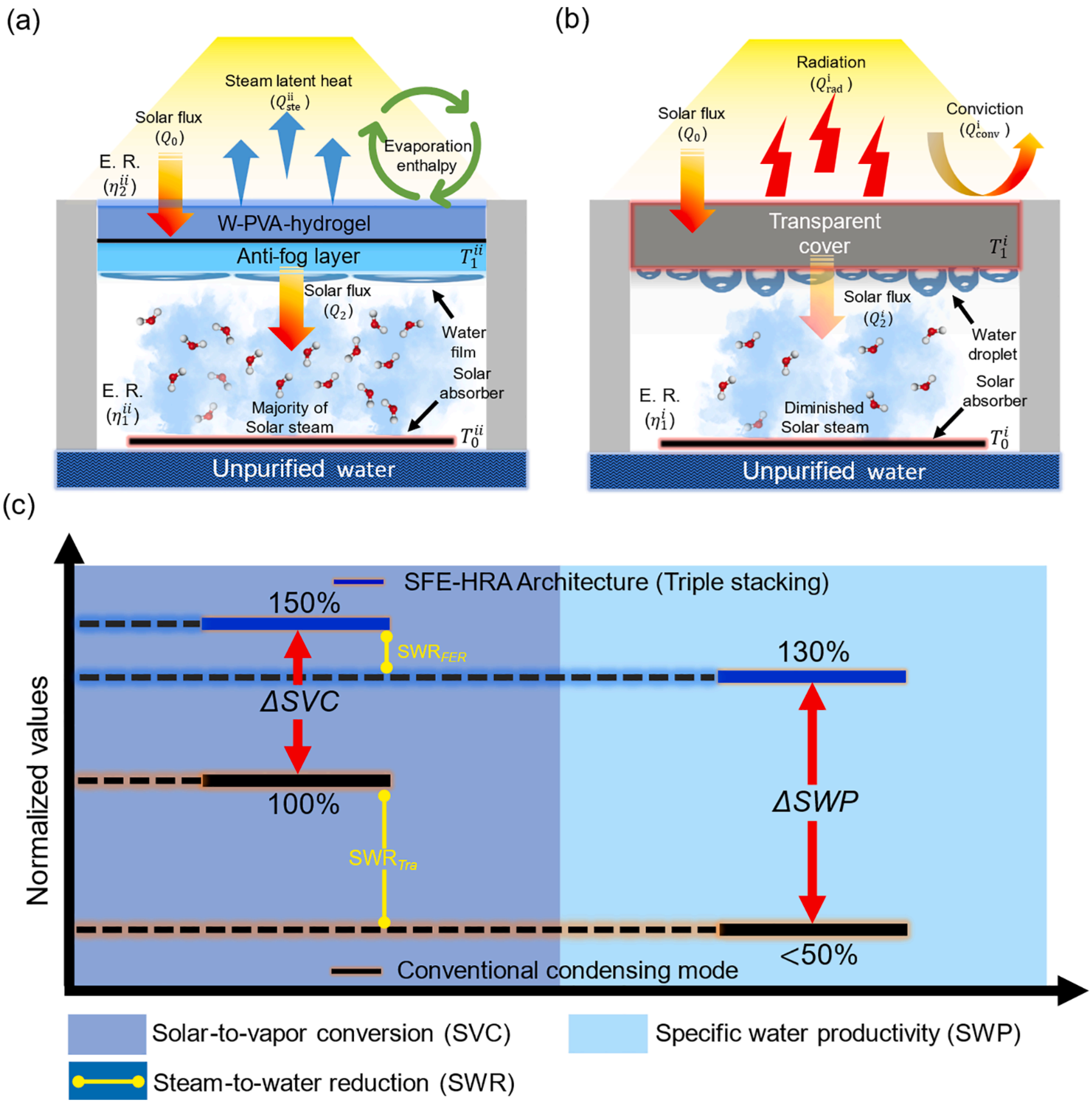

Fig. 1. Schematic diagram illustrating the differences in vapor condensation recovery modes between the SFE-HRA system and conventional solar evaporation–condensation system. (a) Vapor latent heat cycle and light-heat energy balance mechanism of SFE-HRA. (b) Water production efficiency suppression and photo-thermal energy loss mechanisms in transparent condensers. (c) Comparing the solar vapor generation efficiency and the vapor-to-water conversion efficiency of (SFE-HRA)-CSE system and conventional solar evaporation–condensation system (Yellow line represents the conversion efficiency of solar vapor production into liquid water yield in both modes.). (For interpretation of the references to colour in this figure legend, the reader is referred to the web version of this article.)

(PL-MW2000). The entire system, including the (SFE-HRA)-CSE, sealed foam, test water and container, was placed on an electronic balance that automatically recorded the weight. During the evaporation test, room temperature (23.5–24.5 °C) and humidity (45–55 %) were maintained by air conditioning. Calibrated K-type thermocouple (HT-9815 with accuracy of ±1 °C) and hygrometer (CX-601 with humidity resolution of 1 % RH and accuracy of ±5 %) were installed around the solar evaporator to measure the ambient temperature and relative humidity around the solar simulator area. Partition screens were employed to isolate the system from the surrounding environment, preventing any influence from ambient airflow during evaporation. Before each testing cycle, the light intensity on the sample surface was recalibrated using a light power meter to minimize testing errors. During the experiment, the temperature changes on the SFE-HRA surface and water supply layer were measured using a thermocouple (FLIR, TG-267).

2.6. Outdoor test of the 3-(SFE-HRA)-CSE device

The test platform is located on the roof of the Ecological Experiment Building at Tongji University, Shanghai, China. The benchmark 3-(SFE-HRA)-CSE system and the stand-alone acrylic-CSE system have evaporative surfaces facing 90° upwards. The methods used to measure operating temperature, ambient temperature and humidity are the same as the indoor tests. Solar irradiance was measured by a solar intensity meter. The masses of plant fibres and acrylic condensation covers before and after vapor coverage were measured by an electronic mass balance equipped with a windshield.

2.7. Vapor exposure testing

To test the characteristic fogging behaviour of AFM with other transparent substrates at different temperature vapor surfaces, K-type thermocouple was first fixed to the EPE foam surface (0.023 W m^{-1} k^{-1} thermal conductivity) by acrylic adhesive on the bottom side of a 3 × 3 cm^2 PVC film (3 M Scotch Super 88), and the PVC-thermocouple-EPE foam was placed in a 5 × 5 cm^2 transparent acrylic container. A clear round glass vessel is provided at the top to hold the hot water for steam generation. The size-matched transparent substrate is directly exposed

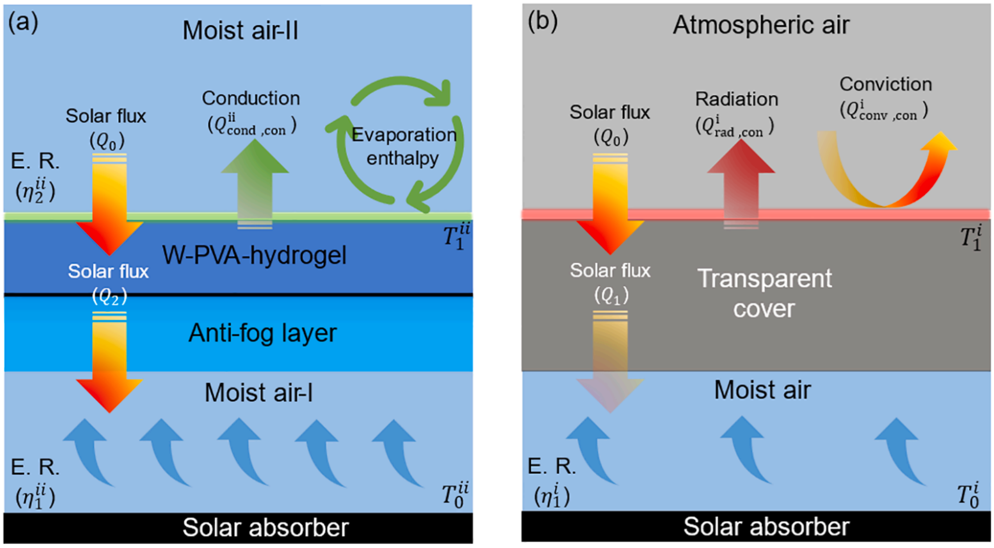

Fig. 2. Schematic diagram of the difference in the photothermal-vapor transfer mechanism between a single-stage SFE-HRA (a) and a conventional condenser (b).

to the surface of the glass container. The effects of fogging behavior on the photothermal conversion performance of the bottom absorber are verified by testing the temperature change on the surface of PVC film. A solar power meter (PL-MW2000) replaced the photothermal conversion device to verify the incident light power variation. The sunlight simulation test standards and equipment are shown in Supplementary Note 2.5.

3. Results and discussion

3.1. Principle and conceptual schematic of the (SFE-HRA)-CSE system

Fig. 1 illustrates the working principles of the (SFE-HRA)-CSE system and conventional condensers with a schematic diagram regarding light-heat energy utilization and mass transfer mechanisms. Details of the material composition and construction of each sub-module of the (SFE-HRA)-CSE system are given in Notes S1 and S2.2. In a front-end solar evaporation system equipped with a single-stage SFE-HRA (Fig. 1a), the hydrophilic membrane at the lower interface of biH-TMNF functions primarily as an anti-fogging layer, preventing vapor condensation droplets generated by the CSE from interfering with the incident light power. By employing in-situ polymerization, the two layers achieve a seamless fit. The flawless integration between the two layers allows the porous hydrogel skeleton to function as an evaporation accelerator. This intricate process capitalizes on the transmitted latent heat of evaporation from the lower interface, thereby efficiently promoting water evaporation both on the surface and in the complex network of pores. This principle enables continuous latent heat recovery and water collection by this stacked SFE-HRA. We confirmed a trade-off between the number of stacked layers and the efficiency of latent heat recycling in the SFE-HRA. Considering the incomplete light transmission properties of the biH-TMNF and the thin water layer, this study limits the maximum number of stacked layers to three in the SFE-HRA.

The benefits of thermal localized solar evaporation technology are undermined by conventional condenser design flaws that limit SWP efficiency (Fig. 1b). Conversely, the innovative SFE-HRA system intelligently harnesses the synergistic thermal effect of water absorption and evaporation within the multi-stage latent heat cycle, obtaining enhanced evaporation and condensation. The surface layer of the transparent WPH backbone in the SFE-HRA system allows for adjustable water input, optimizing the temperature difference between the hot and cold sides. Compared to traditional single-layer condensers that rely solely on passive thermal convection, thermal radiation, and other natural heat dissipation methods to reduce the temperature on the hot side, the SFE-HRA system minimizes latent heat loss from the vapor. It maintains a significant temperature difference with the evaporative side through efficient heat dissipation, enhancing water production efficiency (Fig. 1c). Based on Fig. 1, Fig. 2 provides additional insights into the efficient synergistic photo-thermal management capabilities of the SFE-HRA system, which are compared to a conventional condenser. The SFE-HRA system relies on the transparent bifunctional membrane design of the biH-TMNF to enable the latent heat of the front solar vapor to be recycled multiple times on the light incidence side. By balancing the effect of the number of stages of the SFE-HRA module on the light incidence and latent heat recycling efficiency of the bottom solar evaporator, the optimal number of SFE-HRA stacks is obtained, and the efficiency of the conversion of the front solar vapor to water is dramatically increased. This further extends the miniaturized front-end desalination equipment for cost-effective production with a facilitating effect.

3.2. WPH construction, characterization and evaluation

3.2.1. WPH construction

In SFE-HRA design, we introduced a tailored ultra-transparent homogeneous hydrogel porous skeleton, the WPH. Notably, it is the first innovative proposal to employ a porous hydrogel backbone with transparent optical properties for accelerated solar vapor latent heat circulation from the front end. Three principles guided the WPH construction: 1) Efficient transmission of spectral solar energy and maximum transmission of incident solar light to the bottom surface of the CSE, 2) surface hydrophilicity to facilitate rapid water transport and exhibit salt tolerance, and 3) a multilayer porous and interconnected micro-nano structure to enable efficient interfacial heat transfer and reduce evaporation enthalpy [42,43].

Electrospray-mediated in-situ polymerization and freeze casting prepared the ultrathin hydrophilic WPH with a complex multilayer porous structure (Notes S2.1 and S2.2). The resulting system exhibited a layered architecture with a vertical radial array, as shown in Fig. 3a. The WPH can be securely immobilized on the backside of the anti-fogging membrane (AFM) through strong hydrogen bonds between the two materials, eliminating the need of additional assistance.

Scanning electron microscopy (SEM) images (Fig. 3b-g) revealed that the layered structure of the WPH evaporation films consisted of large vertical hollow arrays (~10 μm). Fig. 3b displays the vertically aligned array structure of WPH. Fig. 3c shows enlarged SEM images highlighting

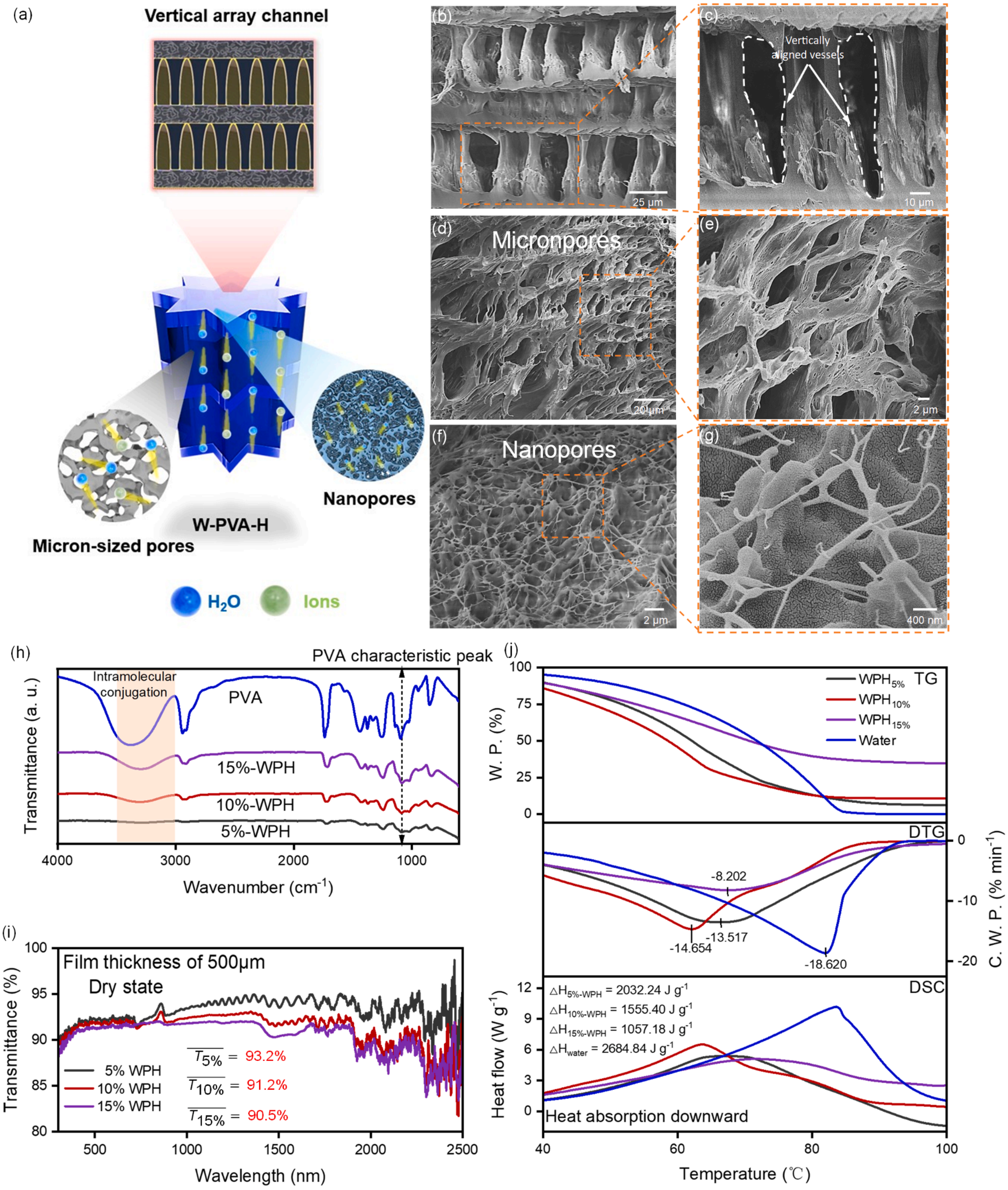

Fig. 3. Characterization and Performance Testing of WPH Water Evaporation Side (a) Schematic diagram illustrating the microstructure and working principle of the WPH transparent evaporator. (b-g) Scanning electron microscope (SEM) images showcasing the multilayer porous structure of the WPH in cross-section. (h) Fourier transform infrared spectra depicting the PVA powder, as well as dried films of 5 %, 10 %, and 15 % WPH. (i) Transmittance analysis of hydrated films with 5 %, 10 %, and 15 % WPH using UV-NIR-diffuse reflectance testing in the range of 300–2500 nm. (j) High-precision simultaneous thermal analysis curves illustrating the energy change during the water phase change in hydrated films of 5 %, 10 %, and 15 % WPH, and in pure water. Unless stated otherwise, the thickness of the WPH films is 500 μm.

the vertically arrayed vessels of WPH. Fig. 3d reveals the micron-scale pores in WPH, along with a further magnified SEM image (Fig. 3e). Fig. 3f showcases the nanoscale pores in WPH, and an additional SEM image with further magnification, showing in Fig. 3g. These hydrated vertical hollow channels efficiently conduct the latent heat of evaporation from the AFM surface, rapidly distributing the thermal energy to pore water and surface water through the solid radial micro-nano pores. Furthermore, the vertically hollow layered porous structure and the hydrophilic skeleton facilitate the prompt transportation of high-salinity brine from the evaporated surface to the non-evaporated surface through convection and diffusion. These unique microstructural features are crucial for ensuring the long-term resistance of the WPH membranes to salt contamination during solar evaporation [42,43].

3.2.2. Evaluation of WPH with various PVA concentrations

Varying concentrations of polyvinyl alcohol hydrogel at 5 %, 10 %, and 15 % were prepared to investigate their impact on the hydrogels' transparent optical properties and evaporation capacity. All films were uniform, with a thickness of 500 μm. Fourier transform infrared spectra confirmed C-O stretching bands at 1,085 cm^{-1}, indicating the successful

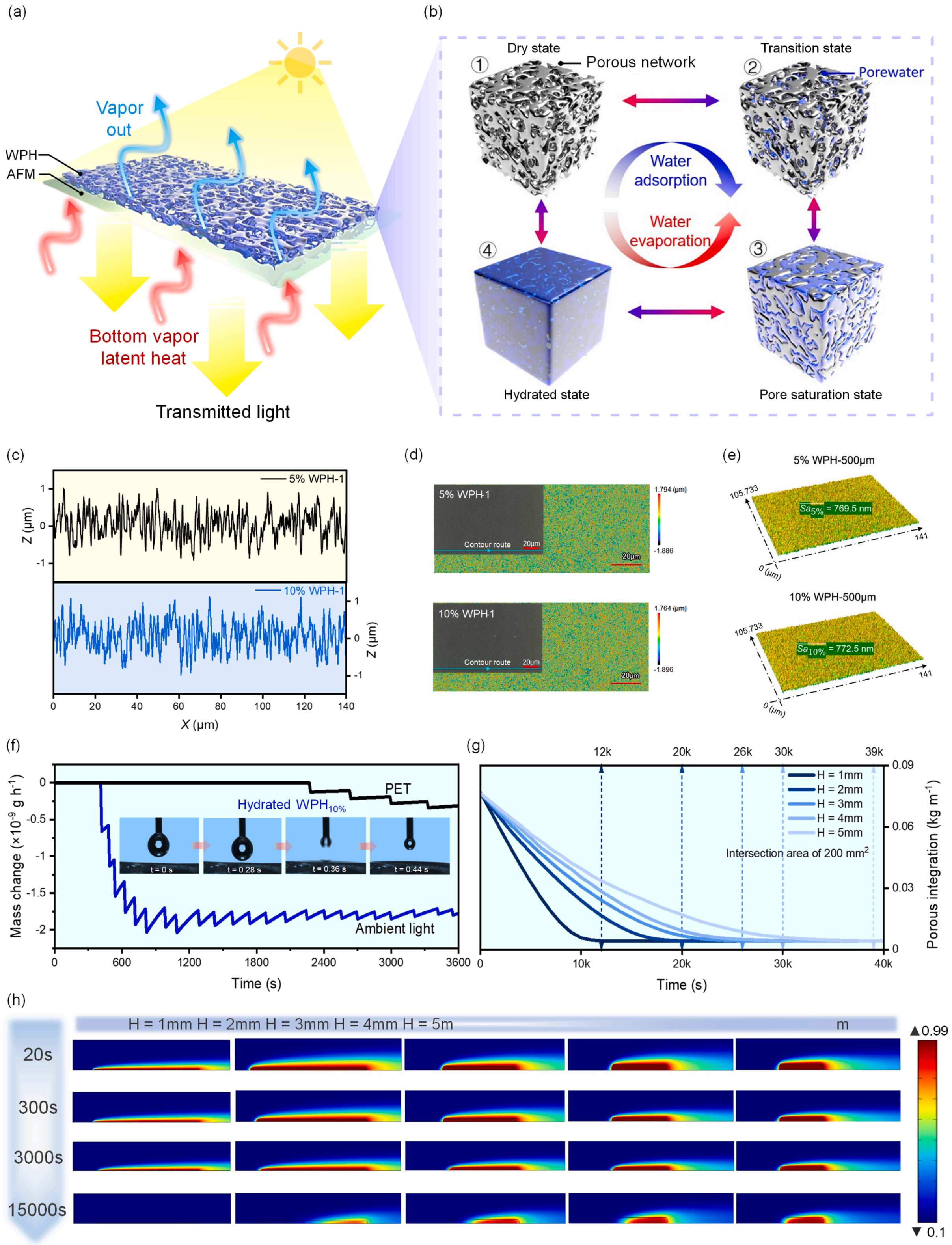

Fig. 4. Characterization of interfacial uniformity of WPH films and simulation of liquid film evaporation with different thicknesses. (a) Schematic diagram illustrating the interfacial transfer mechanism of the light-heat-vapor medium in the vertical direction in a single-stage SFE-HRA. (b) Visualizations of the temporal evolution of hydration state during water absorption/evaporation in the transparent WPH micro-nano water skeleton, which serves as an evaporative enhancement layer. (c) 3D morphological contour lines of the WPH film surface. (d and e) Vertical height and 3D imaging maps with different chromatic aberrations showcasing the surface roughness of WPH. (f) Evaporation performance test comparing the surfaces of infiltrated PET and WPH films under natural illumination, using droplets of the same volume, and contact angle test of hydrated WPH$_{10\%}$. (g) Curve illustrating the moisture content in the pores of the porous media over time. (h) Simulation images displaying the relative humidity of the intercepted porous media at 20, 300, 3,000, and 15,000 s.

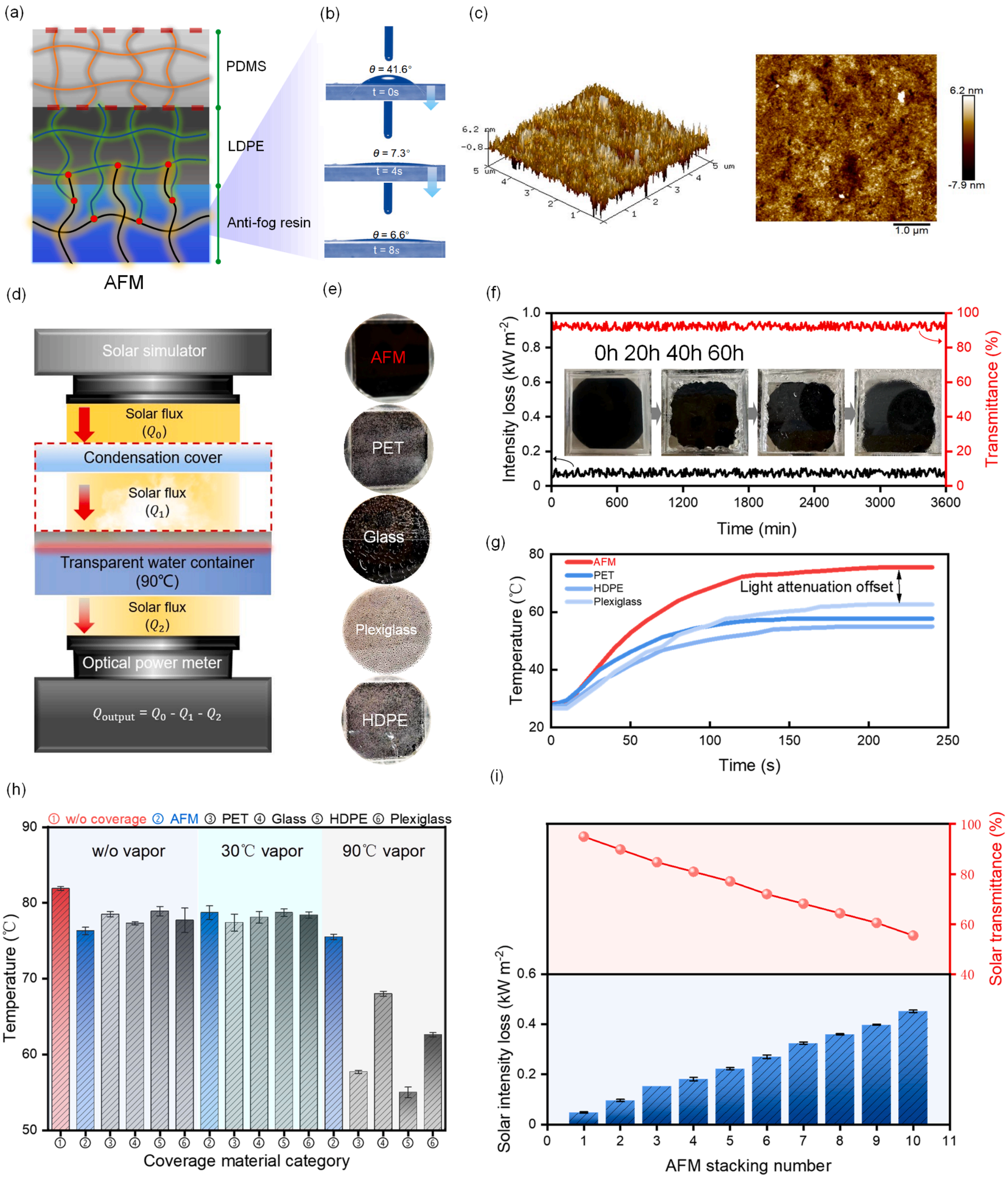

Fig. 5. Characterization of surface properties and anti-fogging performance of a transparent hydrophilic film. (a) Schematic diagram of the anti-fog film. (b) Contact angle test showing good hydrophilicity. (c) AFM test showing the thickness and roughness of the hydrophilic resin layer on the hydrophilic side. (d) Schematic diagram of the effect of interfacial fogging degree on light incidence rate under 90° water vapor exposure for different transparent layers. (e) Optical photograph. (f) Measurement of solar light transmittance change of AFM film under 40 °C water vapor exposure during a testing period of 3600 min (simulating the surface temperature of a conventional solar evaporator). Different transparent materials temperature variation in bottom photothermal conversion performance (g) under 90 °C water vapor exposure, (h) under no water vapor exposure, 30 °C water vapor exposure, and 90 °C water vapor exposure. (i) The influence of AFM stack layers on solar light transmittance.

synthesis of PVA hydrogels (Fig. 3h). The wave number interval from 3,000 cm^{-1} to 3,500 cm^{-1} represents the degree of intramolecular connectivity of the hydroxyl transmission peaks [44,45]. The variation in PVA concentration is depicted through differences in peak shape, with higher PVA concentrations shifting the in-plane deformation vibration of the hydroxyl peaks to lower wave numbers. UV–Vis-NIR spectroscopy (Fig. 3i) was conducted, confirming that all three ratios of hydrated WPH with PVA exhibited high transmittance (>90 %) in the solar spectrum range. Although the stability of the polymer network structure increased, a slight decrease in transmittance was observed with increasing PVA concentration.

Moreover, combining homogeneous micro-nanopores and functional

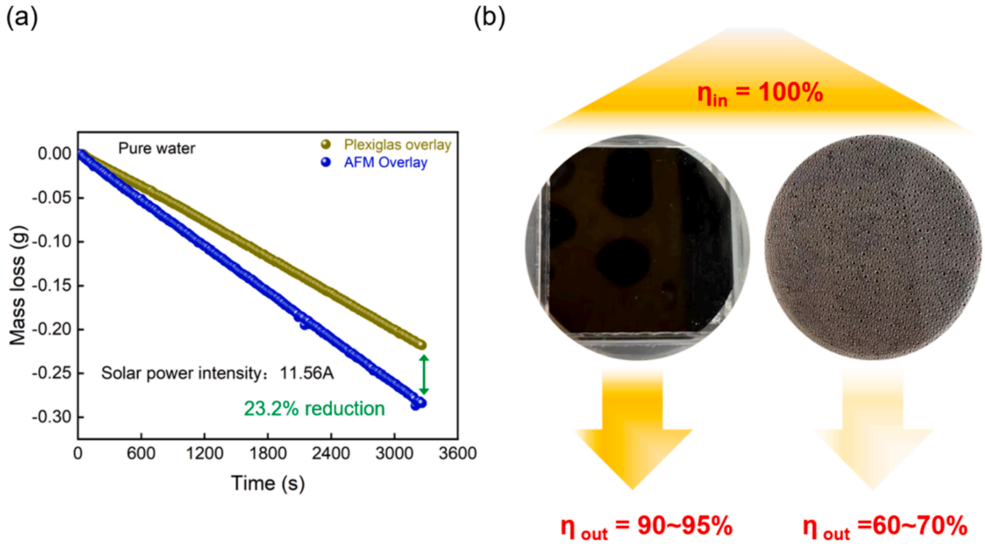

Fig. 6. Solar evaporation performance with AFM and Plexiglass as condensation cover with CSE as bottom solar evaporator (a), and the optical photographs of interfacial condensation behavior of AFM and Plexiglas condensate layer at steam temperature of 100 °C (b).

groups within the WPH can regulate the formation of hydrogen bonds with surrounding water molecules and reduce the energy required for evaporation [39]. A high-precision simultaneous thermal analyzer confirmed the phase energy transition (liquid–gas) of water in different ratios of WPH and pure water. The enthalpy of evaporation for pure water was approximately 2,684.8 J g^{-1}. In contrast, the enthalpies of evaporation for WPH with 5 %, 10 %, and 15 % PVA after hydration were 2032.2 J g^{-1}, 1555.4 J g^{-1}, and 1057.2 J g^{-1}, respectively (Fig. 3j). This result demonstrates that the WPH evaporation film significantly activated the water evaporation. Considering the balance between light transmission, structural stability, and accelerated evaporation, WPH with 10 % PVA was applied for all subsequent tests.

3.2.3. Interfacial uniformity of WPH and liquid film evaporation simulation

Furthermore, we conducted investigations on the surface properties of the WPH film in the SFE-HRA latent heat cycle system (Fig. 4a). The hydrophilic porous WPH film goes through different states, including the dry state, transition state, and pore-filled state, as it absorbs sufficient water and becomes fully hydrated, forming a water skeleton. Surface laser imaging analysis of 5 % and 10 % WPH films demonstrating the homogeneous surface of the WPH film (Fig. 4b). The mechanism behind liquid film evaporation in the SFE-HRA system can be explained from three perspectives: 1) liquid film promotes light transmission; 2) liquid film with more uniform surface energy and evaporation temperature under the same thermal energy transmission; and 3) homogeneous liquid film that reduces the impact of surface ripples and liquid flow on light scattering and reflection [46–48].

The surface 3D morphological contour lines (Fig. 4c) and roughness (Fig. 4d) of the WPH films with 5 % and 10 % PVA were subsequently examined by laser microscopy. White lines in the optical photographs indicate the imaging path of the laser. The arithmetic means height (Sa) of the surfaces for the WPH films with 5 % and 10 % PVA were found at 769.5 nm and 772.5 nm, respectively (Fig. 4e), demonstrating that both WPH films, at their respective PVA concentrations, exhibited highly homogeneous and randomly distributed microscopic fold structures (Figs. S2 and S3). Additionally, the aspect ratios of the surface features of both membranes were determined to be 0.942 and 0.945 (Str), respectively. This indicates that the fold structure of the WPH surface grows anisotropically, effectively reducing the reflection of incident light[18]. Notably, the unique fold structure significantly increases the membrane surface area by 5000 % (Sdr), facilitating rapid evaporation of the attached liquid film and pore water (Table S1).

Further, a hydrophobic PET film and hydrated WPH were used as carrier substrates to carry liquid films with different thicknesses to verify the universality of the above mechanism. Surface contact angle test illustrates that the hydrated WPH film displays super-hydrophilicity, forming a flat, stable liquid film of water molecules on its surface (Fig. 4f). Real-time mass loss measurements indicate that the difference in fluid morphology on the two films significantly affects their evaporation efficiency.

To gain further insight into the impact of liquid distribution patterns on the evaporation rate, we experimented using dry gas flowing through the porous WPH material containing moist air and liquid water under natural laminar flow conditions (Fig. S4) [49,50]. Five different height conditions (H = 1, 2, 3, 4, and 5 mm) represent varying liquid film attachment to the solid surface, ranging from strong to weak hydrophilicity (Note S2.4). The equilibrium point of humidity within the porous material shifts backwards with an increase in liquid film height (Fig. 4g). The equilibrium durations of moisture for the H range of 1–5 mm were determined as 12 k, 20 k, 26 k, 30 k, and 39 k s, respectively. The simulation results (Fig. 4h) align well with the earlier conclusion regarding the impact of liquid morphology on the evaporation rate, particularly the equilibrium point (double arrow dashed line in Fig. 4g). Noteworthy, in actual solar desalination processes, a thinner liquid film accelerates salt crystallization. This highlights the significance of introducing an adjustable convective drive to balance efficient evaporation and desalination performance.

3.3. Properties and anti-fogging performance of AFM

To assess the suitability of the universal AFM for long-term solar distillation processes, contact angle and surface wetting properties were analyzed (Fig. 5a-b and Fig S5). Fig. 5a illustrates the composition of the anti-fog film, which consists of three synergistically combined transparent layers, including a hydrophilic top layer formed by crosslinking of transparent polymer resin, a stretchable intermediate layer made of low-density polyethylene with high elasticity recovery, and a polydimethylsiloxane adhesive bottom layer. Over time, the contact angle sharply decreased from 41.6° to 7.3° within 4 s, demonstrating the AFM's ability to rapidly convert droplets into a liquid film due to its high extensibility (Fig. 5b). Atomic force microscopy imaging techniques indicate that the transparent resin layer deposited with a 6–34 nm thickness, effectively boosting the light transmission incident to the

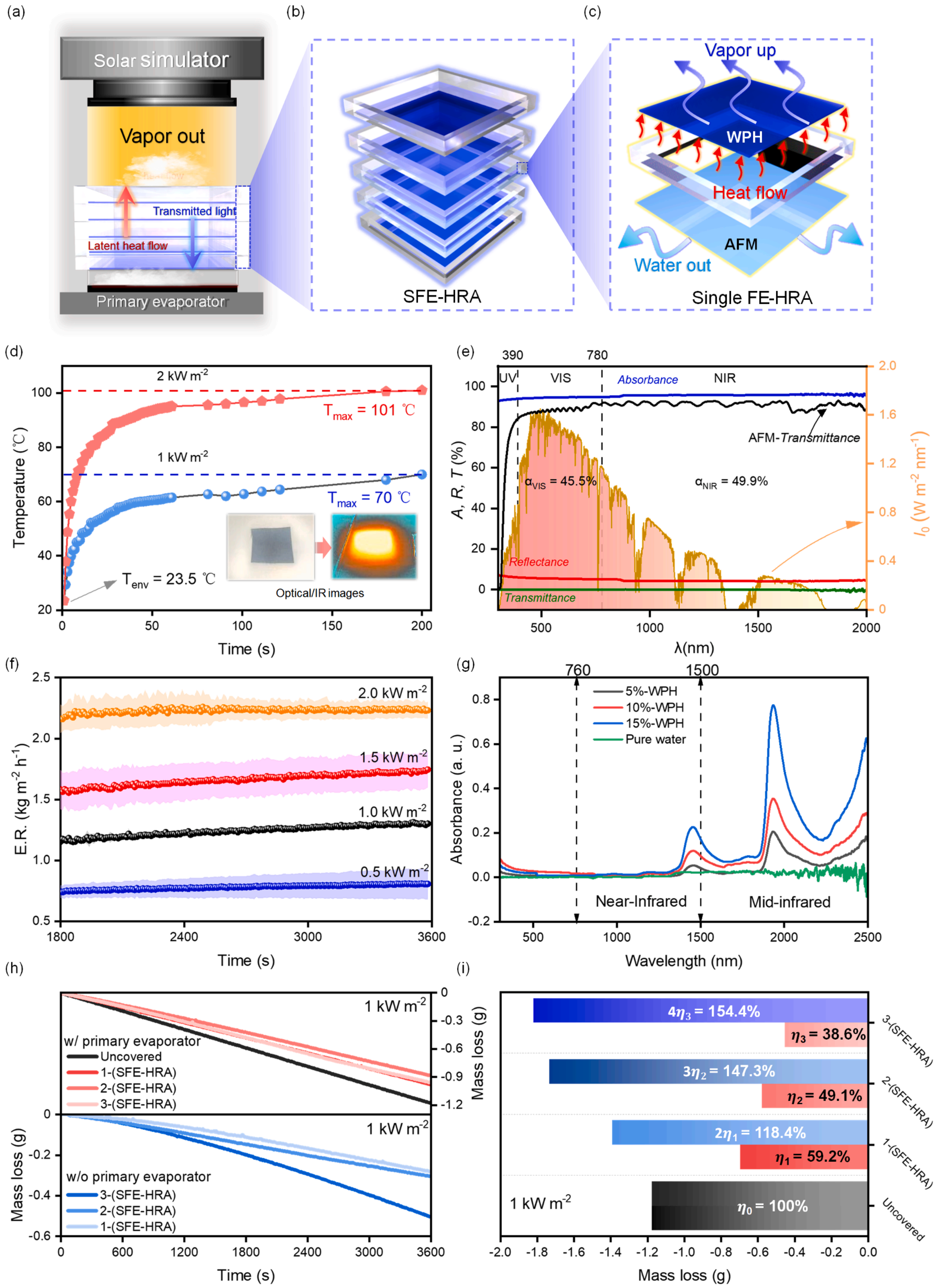

Fig. 7. Construction of a prototype SFE-HRA and its solar thermal evaporation performance. (a) Schematic diagram of the principle of conducting laboratory solar vapor performance tests by stacking SFE-HRAs step by step. (b) Schematic diagram of the stacked SFE-HRAs. (c) Heat and mass transfer mechanisms of each substructure of the single-stage SFE-HRA during the operation of the stacked SFE-HRA-solar evaporation system. (d) Intrinsic photothermal conversion performance test of the black PVC film in CSE and showing the optical and infrared images of the film with 1 cm edge length under simulated light illumination. (e) UV–Vis-NIR spectra. (f) Evaluation of the radiation intensity of the CSE under different solar irradiation (0.5–2 kW m^{-2}). E.R. indicates the evaporation rate. (g) UV–visible-diffuse reflectance testing of 5 %, 10 %, 15 % WPH and pure water. (h) A comparison of the real-time mass loss for SFE-HRA stacks of layers 0, 1, 2, and 3, respectively. (i) Evaluation of evaporation enthalpy recovery efficiency for each stack equivalent at SFE-HRA.

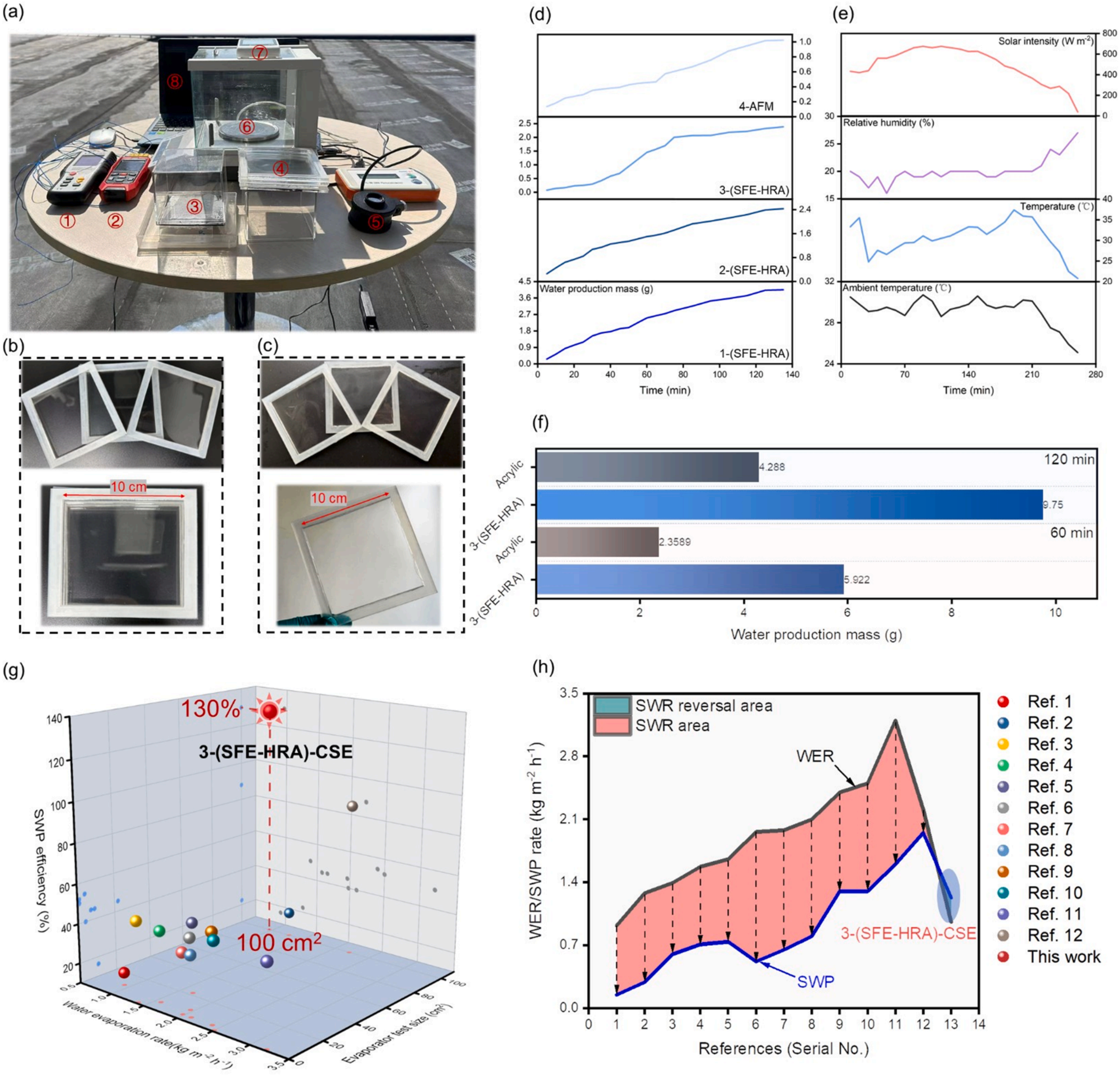

Fig. 8. Outdoor system setup and performance verification of the (SFE-HRA)-CSE with sunlight. (a) Experimental setup. The experimental test rig consisted of (1, 2) two thermocouple meters, (3) a conventional front-end solar evaporation–condensation system based on CSE, (4) a three-stage (SFE-HRA)-CSE device, (5) a solar flux meter (200–11,000 nm), (6) a balance, (7) A high precision temperature and humidity meter and (8) a computer. (b) SFE-HRA frame images for load AFM only. (c) SFE-HRA frame images after loading WPH on the non-anti-fog surface of AFM. (d) SWP rate of 3-(SFE-HRA)-CSE in outdoor experiment. (e) Real-time evolution of the ambient temperature, surface temperature of CSE, air RH, and solar irradiation during the (SFE-HRA)-CSE operation. (f) Comparison of solar water collection mass of 3-(SFE-HRA)-CSE and conventional CSE condensing system at 60 and 120 min. (g) Comparison of WER (X-axis), evaporator test size (Y-axis), and SWP efficiency (Z-axis) with previous reports. (h) Plots of WER and corresponding SWP changes in literature and 3-SFE-HRA-CSE solar desalination systems, with red areas indicating the magnitude of the loss of SWR in other literature and green areas indicating the magnitude of growth of SWR in 3-(SFE-HRA)-CSE. (For interpretation of the references to colour in this figure legend, the reader is referred to the web version of this article.)

bottom CSE (Fig. 5c and Fig S6).

A short-time exposure test was designed to evaluate the fogging behaviour of various materials when exposed to the surface layer of a high-temperature body of water (Fig. 5d and Fig. S7). Optical photographs illustrate the character fogging behaviour of the five transparent layers after being exposed to heated water vapor at 90 °C for 5 min (Fig. 5e). The AFM consistently maintained optical transparency, while all other materials exhibited varying degrees of fogging (Figs. S8 and S9). Although prolonged exposure to vapor from water at 40 °C, the AFM effectively maintained a high total transmittance (>90 %) and consistent optical transparency (Fig. 5f and Fig. S10).

Fig. 5g depicts the impact of four transparent materials on the bottom light absorber during a short-time high humidity exposure test. Over 200 s, the AFM cover layer exhibited the highest light incidence efficiency. The presented AFM exhibits a reflectivity of 5 %-10 % (Fig. 5h-i). Meanwhile, in comparison with the light scattering behavior caused by surface atomization (Fig. 6), which seriously affects the photothermal conversion efficiency of the bottom solar absorber, the light-transmitting micro-liquid film produced by AFM effectively suppresses the decrease in photothermal-vapor generation efficiency (Fig. 6b). Considering the trade-off between latent heat recovery efficiency and the inherent stepwise decay of light reflectivity, further research is required to optimize the number of stacked layers of SFE-HRA. More mechanical stability studies on hydrophilic substrates are needed to explore universal solutions for maintaining fog resistance of transparent materials over time under wet and dynamic conditions [51].

3.4. Proof-of-concept of SFE-HRA and solar evaporation capability

A prototype SFE-HRA setup was established (Fig. 7a-c), and its performance was evaluated under uniform solar illumination provided by a solar simulator at a rate of 1 kW m^{-2} (Note S2.5). Fig. 7a demonstrates the principle of conducting laboratory solar vapor performance tests by stacking SFE-HRAs. It measures the vapor loss rate of the top evaporative layer at each stacking equivalent and calculates the lower limit of photothermal vapor conversion efficiency at that number of layers. One of the SFE-HRA layers was enlarged to construct a single-stage SFE-HRA (Fig. 7b-c). The bottom layer of the stacked SFE-HRA-solar evaporation system consists of a low-cost front-end solar evaporator to generate the initial vapor, and each layer of SFE-HRA is fixed by a 1 mm thick acrylic frame and a 0.5 mm thick flexible silicone mat as a sandwich layer with good airtightness and effective waterproofing. The design thickness of the acrylic frame and silicone pad is the height of the air gap between adjacent SFE-HRAs, which is highly adjustable and used to optimize the total enthalpy recovery efficiency of the SFE-HRA system. Using an infrared camera evaluated the intrinsic photothermal conversion performance of the black PVC film in the dry state (Fig. 7d and Fig. S11). Under simulated light irradiation of 1 kW m^{-2} and 2 kW m^{-2}, the temperature of the central irradiated region of the PVC film reached equilibrium temperatures of 70 °C and 101 °C after 200 s, respectively. The solar absorbance of the PVC film reached 94 % in the wavelength range of 0.3–2.5 μm by UV–Vis-NIR spectra with integrating spheres (Fig. 7e), demonstrating that the PVC film can effectively serve as a photothermal absorber for solar radiation heating of the evaporative layer. Fig. 7e also shows the optical transmittance performance of the AFM film.

Furthermore, CSE revealed a linear trend of evaporation rate at different light intensities ($R^2 > 0.99$, Fig. S12), reaching 1.31 kg $m^{-2}h^{-1}$ at 1 kW m^{-2} (Fig. 7f). Interestingly, unlike the stepped temperature distribution observed in multi-stage passive solar distillation, the temperature of the evaporating layer increased as it approached the light source in the stacked SFE-HRA (Fig. S13). This temperature distribution resulted from solar radiation absorption by the hydrogel in each stage of SFE-HRA (Fig. 7g). The absorbed radiation energy excited the water molecules, causing internal vibration and rotation, leading to an increase in the temperature of the evaporating water layer. Therefore, the thermal energy that did not reach the CSE was initially allocated to the WPH-water layer in the SFE-HRA. Notably, the temperature gradient generated by the outdoor light excitation effect is expected to be significantly weakened due to the difference in the lightweight vision factor between simulated and outdoor sunlight scenes.

We conducted a test on the real-time mass loss of the three-stage SFE-HRA under standard solar intensity (The red line shown in Fig. 7h). The results were consistent with the temperature variation, with the top evaporative layer achieving approximately 75 % of the evaporation performance of the CSE at the first two equivalent SFE-HRA stage. The maximum evaporation rate reached 81 % of the initial efficiency at the third SFE-HRA stage. To determine the respective contributions of the latent heat of evaporation and thermal excitation effects during SFE-HRA operation, we further tested the evaporation performance of each SFE-HRA stage under light without the CSE condition (The blue line shown in Fig. 7h). By subtracting the contribution of evaporation under the morning without the CSE condition from the steady-state mass loss rate, we estimated the total efficiency of latent heat evaporation under each equivalent SFE-HRA stage. Evaporation under CSE conditions is also shown for evaluating the thermal energy contribution provided by the latent heat of evaporation. Considering the real-time photothermal-vapor conversion efficiency as 100 % for the CSE under the no-SFE-HRA condition, the top photothermal-vapor conversion efficiencies for 1-stage SFE-HRA, 2-stage SFE-HRA, and 3-stage SFE-HRA were calculated as 59.2 %, 49.1 %, and 38.6 %, respectively. The total latent heat recovery efficiencies at each SFE-HRA equivalent stage were calculated by multiplying the number of vapor-generating layers, resulting in 118.4 %, 147.3 %, and 154.4 %, respectively (Fig. 7i).

The non-linear evaporation temperature distribution resulting from light transmission decay and thermal excitation effects, along with non-essential structural heat losses, leads to an exponentially decreasing vapor mass flux dominated by the latent heat cycle with the increase in the stage number in the stacked SFE-HRA (Fig. 7i). Black bars indicating the real-time mass loss of the initial evaporator without cover and red bars indicate the proportion of energy provided by latent heat cycle in the top evaporation layer at stack equivalent ($\eta = (M_n - M_n')/M_0$, M_n denotes the loss mass with CSE under n-level stacking, M_n' denotes the loss mass without CSE under n-level stacking, and M_0 denotes the loss mass without covered CSE). The blue bars indicate the total energy efficiency provided by the latent heat cycle of evaporation only (top evaporation efficiency × number of vapors generating layers). The result highlights the significance of optimizing stage number. While there is a notable efficiency gain of approximately 28.9 % when increasing from stage 1 to stage 2 and only 7.1 % from stage 2 to produce 3 in terms of latent heat cycles, it is outweighed by the increased attenuation of incident light and structural heat loss that occur when adding more stages. Moreover, the material cost remains constant.

3.5. Outdoor demonstration of SFE-HRA with sunlight

The outdoor experiments were conducted on the rooftop to validate the practical feasibility of the SFE-HRA (Fig. 8a). A conventional CSE-condensation system with an acrylic layer was set up as a benchmark for comparing water collection efficiency. Using the same fabrication technique, a scaled-up 3-stage AFM and AFM-WPH model measuring 10 cm in length was constructed (Fig. 8b-c). Due to 1) thermal inertia effects in the actual solar irradiation environment, 2) optical attempt factor differences, and 3) conduction heat to volumetric water in the scale-up CSE, a lower initial evaporation rate of 0.96 kg $m^{-2}h^{-1}$ in single CSE was obtained. Fig. 8d-e illustrates the water productivity during the operational period for each stacked layer of the 3-(SFE-HRA)-CSE under an average solar flux intensity of 448.5 W m^{-2}. The outdoor solar water production experiment was conducted in Shanghai from 11:00 a.m. to 1:00p.m. on May 9, 2023. The diagram shows the water mass collected in 2 h. In the first hour, the 3-(SFE-HRA)-CSE collected 5.92 mL of water, achieving an SWP rate of 1.23 kg $m^{-2}h^{-1}$ and a mean SWP efficiency of 130 %. In comparison, the traditional condensation mode collected only 2.35 mL of water with an SWP rate of 0.48 kg $m^{-2}h^{-1}$ (Fig. 8f). Notably, the performance of the SFE-HRA surpassed previously reported natural cooling interface solar vapor generation systems ($\eta = 50$ %) and electric water production equipment with complex vacuum systems ($\eta = 93$ %, 0.17 atm) (Table S2) [18,52].

Additionally, this study presents the first outdoor validation of the scalable front-end solar vapor-latent heat-water recovery system on a surface area of up to 100 cm^2 (Table S2). Existing reports have primarily focused on the modular potential of evaporative materials at the microscale (<1 cm^2) [13,33]. Building upon this, we compared and validated the progress of the (SFE-HRA)-CSE system against other studies based on three key aspects: evaporator size, WER, and SWP efficiency (Fig. 8g) [39,43,45,53]. Our analysis concentrated on productivity metrics, strategies to overcome the limitations of single-stage systems, and scalability. Among the three parameters, the SFE-HRA device achieved optimal productivity efficiency with its light-incidence loss suppression and front-end vapor cycling strategy. Specifically, the (SFE-HRA)-CSE system exhibited an increasing trend in solar vapor-to-water conversion, even with an initial vapor volume significantly lower than that of high-performance evaporators (WER>2 kg $m^{-2}h^{-1}$) (Table S2). Ultimately, the liquid water yield surpassed that of high-performance evaporators (Fig. 8h).

This development of the integrated biH-TMNF and construction of the SFE-HRA system is a promising avenue for boosting front-end solar vapor-to-water conversion. The fundamental understanding of materials, optics, heat dissipation and structure is central to improving solar

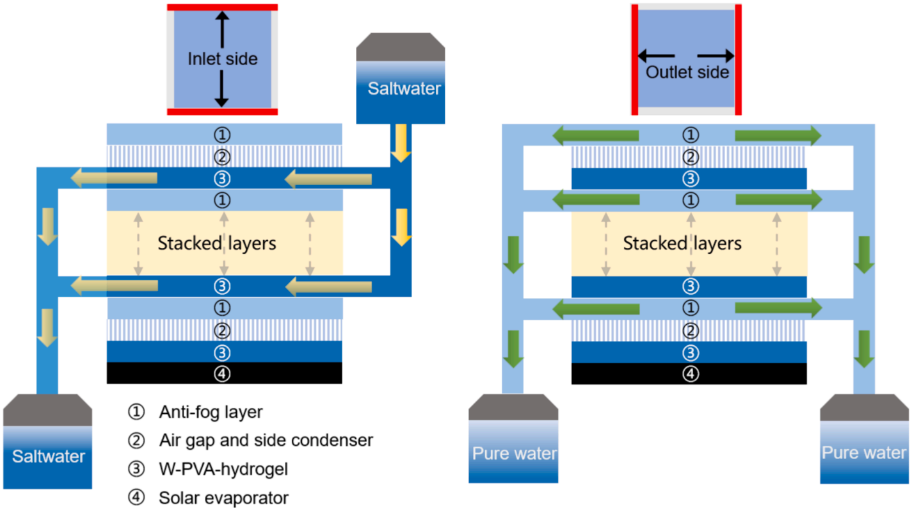

Fig. 9. Schematic diagram of a multi-stack SFE-HRA coupled high-performance front-end solar evaporator desalination-water recovery process facilitated by adjustable convection drive units.

vapor-to-water rates. The solution in this work has eliminated the need for complex pump and control systems, high-energy electrical inputs, and pressurized air-cooling systems. The heat dissipation and condensation of stacked latent heat cycles and the interfacial evaporation can be efficiently triggered and proceeded in the SFE-HRA system. The promotion of latent heat cycle and water harvesting efficiency by this interface design includes the integrated molecular level multifunctional material design [43], adjustable convection drive (Fig. 9) [4] and long-term anti-fogging strategies in complex environments [51], enabling the SFE-HRA system to address the remained challenges of solving the water-energy nexus. Different from the development of high-performance evaporation materials with ultra-low evaporation enthalpies [12,13,23,39,44] and the advances in photo-molecular effects that have the potential to improve front-end evaporation performance [9], the SFE-HRA boosted the vapor-to-water conversion, which is another achievement that promotes efficient solar clean water production.

4. Conclusion

A versatile strategy is proposed to achieve highly efficient front-end solar vapor latent heat recovery and boost solar vapor-to-water conversion. It utilizes a multi-stage micro-liquid film condensation module with high optical transmission properties and a local water activation module to correct the negative chain effect between incident light attenuation and low condensation efficiency and latent heat loss induced in the liquid–vapor-liquid phase transition space in the solar evaporation–condensation system. The SFE-HRA system is designed based on a micro-nano biH-TMNF, which functionalized as a circulatable front-end vapor condensation cooling component, integrating a liquid film condensation module with two-phase functionalization and a porous hydrogel module. Its integration with CSE enables the stacked (SFE-HRA)-CSE system to increase solar vapor production by 150 % and improve condensate recovery by 200–300 %. The critical role of interface engineering design in promoting the efficiency of the latent heat cycle and water harvesting has been emphasized. The (SFE-HRA)-CSE system achieved an unprecedented SWP efficiency of 130 %, surpassing the SWP of all the reported front evaporators. This achievement is of significant potential to pave the way for efficient and sustainable solar clean water production.

CRediT authorship contribution statement

Shuai Peng: Writing – original draft, Methodology, Investigation, Formal analysis, Conceptualization. **Shi-Hai Deng:** Writing – original draft, Methodology, Investigation, Formal analysis, Data curation. **Longqian Xu:** Writing – review & editing, Methodology, Formal analysis. **Huu Hao Ngo:** Writing – review & editing, Supervision, Methodology, Investigation, Conceptualization. **Pengkang Jin:** Writing – review & editing, Methodology, Formal analysis. **Wenshan Guo:** Writing – review & editing, Formal analysis, Data curation. **Zuofeng Chen:** Writing – review & editing, Supervision, Project administration, Methodology, Investigation. **Deli Wu:** Writing – review & editing, Supervision, Project administration, Methodology, Investigation.

Declaration of competing interest

The authors declare that they have no known competing financial interests or personal relationships that could have appeared to influence the work reported in this paper.

Data availability

All data supporting the current study's findings are available within the Article and its Supplementary Information. Any additional data are available from the corresponding authors upon reasonable request.

Acknowledgments

This research was financially supported by the National Key R&D Program of China (2018YFC1903202), the National Natural Science Foundation of China (52170091 and 52106107), and the Young Talent Support Plan of Xi'an Jiaotong University (No. HJ6J008). The authors acknowledge the support of Xi'an Jiaotong University for the use of the COMSOL Multiphysics Version 6.0 copyright.

Appendix A. Supplementary data

Supplementary data to this article can be found online at https://doi.org/10.1016/j.cej.2024.154040.

References

[1] P. Greve, T. Kahil, J. Mochizuki, T. Schinko, Y. Satoh, P. Burek, G. Fischer, S. Tramberend, R. Burtscher, S. Langan, Y. Wada, Global assessment of water

challenges under uncertainty in water scarcity projections, Nat. Sustain. 1 (9) (2018) 486–494, https://doi.org/10.1038/s41893-018-0134-9.

[2] F. Dolan, J. Lamontagne, R. Link, M. Hejazi, P. Reed, J. Edmonds, Evaluating the economic impact of water scarcity in a changing world, Nat. Commun. 12 (1) (2021), https://doi.org/10.1038/s41467-021-22194-0.

[3] V. Velmurugan, M. Gopalakrishnan, R. Raghu, K. Srithar, Single basin solar still with fin for enhancing productivity, Energ. Convers. Manage. 49 (10) (2008) 2602–2608, https://doi.org/10.1016/j.enconman.2008.05.010.

[4] A.E. Kabeel, Performance of solar still with a concave wick evaporation surface, Energy 34 (10) (2009) 1504–1509, https://doi.org/10.1016/j.energy.2009.06.050.

[5] M.N. Sawka, S.N. Cheuvront, R. Carter, Human water needs, Nutr. Rev. 63 (6) (2005) S30–S39, https://doi.org/10.1301/nr.2005.jun.S30-S39.

[6] E. Chiavazzo, Critical aspects to enable viable solar-driven evaporative technologies for water treatment, Nat. Commun. 13 (1) (2022), https://doi.org/10.1038/s41467-022-33533-0.

[7] G. Ni, G. Li, S.V. Boriskina, H. Li, W. Yang, T. Zhang, G. Chen, Steam generation under one sun enabled by a floating structure with thermal concentration, Nat. Energy 1 (9) (2016) 16126, https://doi.org/10.1038/nenergy.2016.126.

[8] L. Zhou, Y. Tan, J. Wang, W. Xu, Y. Yuan, W. Cai, S. Zhu, J. Zhu, 3D self-assembly of aluminium nanoparticles for plasmon-enhanced solar desalination, Nat. Photonics 10 (6) (2016) 393–398, https://doi.org/10.1038/nphoton.2016.75.

[9] X.M. Han, L.V. Besteiro, C.S.L. Koh, H.K. Lee, I.Y. Phang, G.C. Phan-Quang, J.Y. Ng, H.Y.F. Sim, C.L. Lay, A. Govorov, X.Y. Ling, Intensifying heat using MOF-isolated graphene for solar-driven seawater desalination at 98% solar-to-thermal efficiency, Adv. Funct. Mater. 31 (13) (2021) 202008904, https://doi.org/10.1002/adfm.202008904.

[10] S.C. Singh, M. ElKabbash, Z. Li, X. Li, B. Regmi, M. Madsen, S.A. Jalil, Z. Zhan, J. Zhang, C. Guo, Solar-trackable super-wicking black metal panel for photothermal water sanitation, Nat. Sustain. 3 (11) (2020) 938–946, https://doi.org/10.1038/s41893-020-0566-x.

[11] H. Liu, C.J. Chen, G. Chen, Y.D. Kuang, X.P. Zhao, J.W. Song, C. Jia, X. Xu, E. Hitz, H. Xie, S. Wang, F. Jiang, T. Li, Y.J. Li, A. Gong, R.G. Yang, S. Das, L.B. Hu, High-performance solar steam device with layered channels: artificial tree with a reversed design, Adv. Energy Mater. 8 (8) (2018) 1701616, https://doi.org/10.1002/aenm.201701616.

[12] F.B. Zhu, L.Q. Wang, B. Demir, M. An, Z.L. Wu, J. Yin, R. Xiao, Q. Zheng, J. Qian, Accelerating solar desalination in brine through ion activated hierarchically porous polyion complex hydrogels, Mater. Horiz. 7 (12) (2020) 3187–3195, https://doi.org/10.1039/d0mh01259a.

[13] L. Wu, Z.C. Dong, Z.R. Cai, T. Ganapathy, N.X. Fang, C.X. Li, C.L. Yu, Y. Zhang, Y. L. Song, Highly efficient three-dimensional solar evaporator for high salinity desalination by localized crystallization, Nat. Commun. 11 (1) (2020) 521, https://doi.org/10.1038/s41467-020-14366-1.

[14] H. Liang, Q. Liao, N. Chen, Y. Liang, G. Lv, P. Zhang, B. Lu, L. Qu, Thermal efficiency of solar steam generation approaching 100 % through capillary water transport, Angew. Chem. Int. Ed. 58 (52) (2019) 19041–19046, https://doi.org/10.1002/anie.201911457.

[15] X.Q. Li, J.L. Li, J.Y. Lu, N. Xu, C.L. Chen, X.Z. Min, B. Zhu, H.X. Li, L. Zhou, S. N. Zhu, T.J. Zhang, J. Zhu, Enhancement of interfacial solar vapor generation by environmental energy, Joule 2 (7) (2018) 1331–1338, https://doi.org/10.1016/j.joule.2018.04.004.

[16] X. Wu, Z.Q. Wu, Y.D. Wang, T. Gao, Q. Li, H.L. Xu, All-cold evaporation under one sun with zero energy loss by using a heatsink inspired solar evaporator, Adv. Sci. 8 (7) (2021) 2002501, https://doi.org/10.1002/advs.202002501.

[17] H. Ghasemi, G. Ni, A.M. Marconnet, J. Loomis, S. Yerci, N. Miljkovic, G. Chen, Solar steam generation by heat localization, Nat. Commun. 5 (2014) 4449, https://doi.org/10.1038/ncomms5449.

[18] H.Z. Yao, P.P. Zhang, C. Yang, Q.H. Liao, X.Z. Hao, Y.X. Huang, M. Zhang, X. B. Wang, T.Y. Lin, H.H. Cheng, J.Y. Yuan, L.T. Qu, Janus-interface engineering boosting solar steam towards high-efficiency water collection, Energy Environ. Sci. 14 (10) (2021) 5330–5338, https://doi.org/10.1039/d1ee01381e.

[19] D. Wei, C. Wang, J. Zhang, H. Zhao, Y. Asakura, M. Eguchi, X. Xu, Y. Yamauchi, Water activation in solar-powered vapor generation, Adv. Mater. 35 (47) (2023) 2212100, https://doi.org/10.1002/adma.202212100.

[20] C. Wang, K. Xu, G. Shi, D. Wei, Water Skin effect and arched double-sided evaporation for boosting all-weather high salinity desalination, Adv. Energy Mater. 13 (21) (2023) 2300134, https://doi.org/10.1002/aenm.202300134.

[21] K. Xu, C. Wang, Z. Li, S. Wu, J. Wang, Salt Mitigation strategies of solar-driven interfacial desalination, Adv. Funct. Mater. 31 (8) (2021) 2007855, https://doi.org/10.1002/adfm.202007855.

[22] D. Wei, C. Wang, G. Shi, J. Zhang, F. Wang, P. Tan, Z. Zhao, Y. Xie, Enabling self-adaptive water-energy-balance of photothermal water diode evaporator: dynamically maximizing energy utilization under the ever-changing sunlight, Adv. Mater. 36 (18) (2024) 2309507, https://doi.org/10.1002/adma.202309507.

[23] N. Xu, J. Li, C. Finnerty, Y. Song, L. Zhou, B. Zhu, P. Wang, B. Mi, J. Zhu, Going beyond efficiency for solar evaporation, Nat. Water 1 (6) (2023) 494–501, https://doi.org/10.1038/s44221-023-00086-5.

[24] W. Huang, P. Su, Y. Cao, C. Li, D. Chen, X. Tian, Y. Su, B. Qiao, J. Tu, X. Wang, Three-dimensional hierarchical CuxS-based evaporator for high-efficiency multifunctional solar distillation, Nano Energy 69 (2020) 104465, https://doi.org/10.1016/j.nanoen.2020.104465.

[25] G. Ni, S.H. Zandavi, S.M. Javid, S.V. Boriskina, T.A. Cooper, G. Chen, A salt-rejecting floating solar still for low-cost desalination, Environ. Sci. Technol. 11 (6) (2018) 1510–1519, https://doi.org/10.1039/c8ee00220g.

[26] Y.X. Zhang, T. Xiong, D.K. Nandakumar, S.C. Tan, Structure architecting for salt-rejecting solar interfacial desalination to achieve high-performance evaporation with in situ energy generation, Adv. Sci. 7 (9) (2020) 1903478, https://doi.org/10.1002/advs.201903478.

[27] X. Wang, Z. Lin, J. Gao, Z. Xu, X. Li, N. Xu, J. Li, Y. Song, H. Fu, W. Zhao, S. Wang, B. Zhu, R. Wang, J. Zhu, Solar steam-driven membrane filtration for high flux water purification, Nat. Water 1 (4) (2023) 391–398, https://doi.org/10.1038/s44221-023-00059-8.

[28] E. Chiavazzo, M. Morciano, F. Viglino, M. Fasano, P. Asinari, Passive solar high-yield seawater desalination by modular and low-cost distillation, Nat. Sustain. 1 (12) (2018) 763–772, https://doi.org/10.1038/s41893-018-0186-x.

[29] W. Wang, Y. Shi, C. Zhang, S. Hong, L. Shi, J. Chang, R. Li, Y. Jin, C. Ong, S. Zhuo, P. Wang, Simultaneous production of fresh water and electricity via multistage solar photovoltaic membrane distillation, Nat. Commun. 10 (1) (2019) 3012, https://doi.org/10.1038/s41467-019-10817-6.

[30] M.W. Shahzad, M. Burhan, L. Ang, K.C. Ng, Energy-water-environment nexus underpinning future desalination sustainability, Desalination 413 (2017) 52–64, https://doi.org/10.1016/j.desal.2017.03.009.

[31] Z. Wang, Y. Liu, P. Tao, Q. Shen, N. Yi, F. Zhang, Q. Liu, C. Song, D. Zhang, W. Shang, T. Deng, Bio-inspired evaporation through plasmonic film of Nanoparticles at the air–water interface, Small 10 (16) (2014) 3234–3239, https://doi.org/10.1002/smll.201401071.

[32] K. Bae, G. Kang, S.K. Cho, W. Park, K. Kim, W.J. Padilla, Flexible thin-film black gold membranes with ultrabroadband plasmonic nanofocusing for efficient solar vapour generation, Nat. Commun. 6 (1) (2015) 10103, https://doi.org/10.1038/ncomms10103.

[33] Y. Guo, X. Zhao, F. Zhao, Z. Jiao, X. Zhou, G. Yu, Tailoring surface wetting states for ultrafast solar-driven water evaporation, Energy Environ. Sci. 13 (7) (2020) 2087–2095, https://doi.org/10.1039/D0EE00399A.

[34] Z.Y. Xu, L.N. Zhang, L. Zhao, B.J. Li, B. Bhatia, C.X. Wang, K.L. Wilke, Y. Song, O. Labban, J.H. Lienhard, R.Z. Wang, E.N. Wang, Ultrahigh-efficiency desalination via a thermally-localized multistage solar still, Energy Environ. Sci. 13 (3) (2020) 830–839, https://doi.org/10.1039/c9ee04122b.

[35] R. Li, Y. Shi, M. Wu, S. Hong, P. Wang, Photovoltaic panel cooling by atmospheric water sorption–evaporation cycle, Nat. Sustain. 3 (8) (2020) 636–643, https://doi.org/10.1038/s41893-020-0535-4.

[36] T.A. Cooper, S.H. Zandavi, G.W. Ni, Y. Tsurimaki, Y. Huang, S.V. Boriskina, G. Chen, Contactless steam generation and superheating under one sun illumination, Nat. Commun. 9 (2018) 5086, https://doi.org/10.1038/s41467-018-07494-2.

[37] Z.J. Liu, H.M. Song, D.X. Ji, C.Y. Li, A. Cheney, Y.H. Liu, N. Zhang, X. Zeng, B. R. Chen, J. Gao, Y.S. Li, X. Liu, D. Aga, S.H. Jiang, Z.F. Yu, Q.Q. Gan, Extremely cost-effective and efficient solar vapor generation under nonconcentrated illumination using thermally isolated black paper, Glob. Chall. 1 (2) (2017) 1600003, https://doi.org/10.1002/gch2.201600003.

[38] L.B. Zhang, B. Tang, J.B. Wu, R.Y. Li, P. Wang, Hydrophobic light-to-heat conversion membranes with self-healing ability for interfacial solar heating, Adv. Mater. 27 (33) (2015) 4889–4894, https://doi.org/10.1002/adma.201502362.

[39] F. Zhao, X. Zhou, Y. Shi, X. Qian, M. Alexander, X. Zhao, S. Mendez, R. Yang, L. Qu, G. Yu, Highly efficient solar vapour generation via hierarchically nanostructured gels, Nat. Nanotechnol. 13 (6) (2018) 489–495, https://doi.org/10.1038/s41565-018-0097-z.

[40] F. Gong, H. Li, W. Wang, J. Huang, D. Xia, J. Liao, M. Wu, D.V. Papavassiliou, Scalable, eco-friendly and ultrafast solar steam generators based on one-step melamine-derived carbon sponges toward water purification, Nano Energy 58 (2019) 322–330, https://doi.org/10.1016/j.nanoen.2019.01.044.

[41] P.P. Zhang, Q.H. Liao, H.Z. Yao, H.H. Cheng, Y.X. Huang, C. Yang, L. Jiang, L. T. Qu, Three-dimensional water evaporation on a macroporous vertically aligned graphene pillar array under one sun, J. Mater. Chem. A 6 (31) (2018) 15303–15309, https://doi.org/10.1039/c8ta05412f.

[42] S.M. He, C.J. Chen, Y.D. Kuang, R.Y. Mi, Y. Liu, Y. Pei, W.Q. Kong, W.T. Gan, H. Xie, E. Hitz, C. Jia, X. Chen, A. Gong, J.M. Liao, J. Li, Z.J. Ren, B. Yang, S. Das, L. B. Hu, Nature-inspired salt resistant bimodal porous solar evaporator for efficient and stable water desalination, Energy Environ. Sci. 12 (5) (2019) 1558–1567, https://doi.org/10.1039/c9ee00945k.

[43] X.H. Liu, F.X. Chen, Y.K. Li, H.J. Jiang, D.D. Mishra, F. Yu, Z.H. Chen, C.Q. Hu, Y. Chen, L.T. Qu, W.T. Zheng, 3D hydrogel evaporator with vertical radiant vessels breaking the trade-off between thermal localization and salt resistance for solar desalination of high-salinity, Adv. Mater. 34 (36) (2022) 2203137, https://doi.org/10.1002/adma.202203137.

[44] X. Zhou, F. Zhao, Y. Guo, Y. Zhang, G. Yu, A hydrogel-based antifouling solar evaporator for highly efficient water desalination, Energy Environ. Sci. 11 (8) (2018) 1985–1992, https://doi.org/10.1039/C8EE00567B.

[45] F. Zhao, Y. Guo, X. Zhou, W. Shi, G. Yu, Materials for solar-powered water evaporation, Nat. Rev. Mater. 5 (5) (2020) 388–401, https://doi.org/10.1038/s41578-020-0182-4.

[46] S. Sbarra, L. Waquier, S. Suffit, A. Lemaitre, I. Favero, Optomechanical measurement of single nanodroplet evaporation with millisecond time-resolution, Nat. Commun. 13 (1) (2022) 6462, https://doi.org/10.1038/s41467-022-34219-3.

[47] G.G. Wells, E. Ruiz-Gutierrez, Y. Le Lirzin, A. Nourry, B.V. Orme, M. Pradas, R. Ledesma-Aguilar, Snap evaporation of droplets on smooth topographies, Nat. Commun. 9 (2018) 1380, https://doi.org/10.1038/s41467-018-03840-6.

[48] M.J. Liu, S.T. Wang, L. Jiang, Nature-inspired superwettability systems, Nat. Rev. Mater. 2 (7) (2017) 17036, https://doi.org/10.1038/natrevmats.2017.36.

[49] A.K. Datta, Porous media approaches to studying simultaneous heat and mass transfer in food processes. I: Problem formulations, *J. Food. Eng.* 80 (1) (2007) 80–95, https://doi.org/10.1016/j.jfoodeng.2006.05.013.

[50] A. Halder, A. Dhall, A.K. Datta, Modeling transport in porous media with phase change: applications to food processing, J. Heat. Trans-t. Asme. 133 (3) (2011) 031010, https://doi.org/10.1115/1.4002463.

[51] S.T. Lin, Y.Y. Yang, J.H. Ni, Y. Tsurimaki, X.Y. Liu, B.Y. Lu, Y.D. Tu, J.W. Zhou, X. H. Zhao, G. Chen, Stretchable anti-fogging tapes for diverse transparent materials, Adv. Funct. Mater. 31 (36) (2021) 2103551, https://doi.org/10.1002/adfm.202103551.

[52] W.G. Li, Z. Li, K. Bertelsmann, D.E. Fan, Portable low-pressure solar steaming-collection unisystem with polypyrrole origamis, Adv. Mater. 31 (29) (2019) 1900720, https://doi.org/10.1002/adma.201900720.

[53] Y. Tu, G. Chen, Photomolecular effect: visible light absorption at water-vapor interface, arXiv preprint arXiv:2202. 10646 (2022). doi: 10.1038/s41467-018-03840-6.